PHOTONICS Research

Resonance-assisted light–control–light characteristics of SnS_2 on a microfiber knot resonator with fast response

Huihui Lu,[1,2,†] Zhongmin Wang,[1,2,†] Zhijin Huang,[1,2] Jun Tao,[1,2] Hanqing Xiong,[1,2] Wentao Qiu,[1,2,3] Heyuan Guan,[1,2,4] Huazhuo Dong,[1,2] Jiangli Dong,[1,2] Wenguo Zhu,[1,2] Jianhui Yu,[1,2] Yongchun Zhong,[1,2] Yunhan Luo,[1,2] Jun Zhang,[1,2] and Zhe Chen[1,2]

[1]Guangdong Provincial Key Laboratory of Optical Fiber Sensing and Communications, Department of Optoelectronic Engineering, Jinan University, Guangzhou 510632, China
[2]Key Laboratory of Optoelectronic Information and Sensing Technologies of Guangdong Higher Education Institutes, Jinan University, Guangzhou 510632, China
[3]e-mail: qiuwentao@jnu.edu.cn
[4]e-mail: ttguanheyuan@jnu.edu.cn

Received 4 October 2018; accepted 8 October 2018; posted 12 October 2018 (Doc. ID 347500); published 19 November 2018

An all-optical light–control–light functionality with the structure of a microfiber knot resonator (MKR) coated with tin disulfide (SnS_2) nanosheets is experimentally demonstrated. The evanescent light in the MKR [with a resonance Q of ~59,000 and an extinction ratio (ER) of ~26 dB] is exploited to enhance light–matter interaction by coating a two-dimensional material SnS_2 nanosheet onto it. Thanks to the enhanced light–matter interaction and the strong absorption property of SnS_2, the transmitted optical power can be tuned quasi-linearly with an external violet pump light power, where a transmitted optical power variation rate ΔT with respect to the violet light power of ~0.22 dB/mW is obtained. In addition, the MKR structure possessing multiple resonances enables a direct experimental demonstration of the relationship between resonance properties (such as Q and ER), and the obtained ΔT variation rate with respect to the violet light power. It verifies experimentally that a higher resonance Q and a larger ER can lead to a higher ΔT variation rate. In terms of the operating speed, this device runs as fast as ~3.2 ms. This kind of all-optical light–control–light functional structure may find applications in future all-optical circuitry, handheld fiber sensors, etc.

https://doi.org/10.1364/PRJ.6.001137

1. INTRODUCTION

Modern high-performance systems are built by the combination of electronic and photonic components in order to take advantage of each [1,2]. Among different photonic components, a resonant-based structure such as a microfiber knot resonator (MKR) is an important one that finds applications in sensors [3], lasers [4], filters [5], etc. An MKR is a microscopic loop elastically bent by submicrometer silica wire usually with a loop diameter of several or hundreds of micrometers. The submicrometer silica wires can be easily obtained from a tapered microfiber (MF), which has a thinned core size that enables light leakage outside the waveguide core [6,7]. Particularly, the large fraction of evanescent light, when it is combined with materials whose property can be tuned by light [8–10], can achieve a large panel of all-optical devices with different functionalities [11].

Two-dimensional (2D) materials are excellent candidates to be combined with fiber-optic components since their properties can be tuned by light and their atomically thin thickness can facilitate structure fabrications. In addition, there are whole large 2D materials families such as monoelemental graphene [12,13], antimonene [14–16], and phosphorene [17,18]. Few-layer antimonene-decorated MF employed as an optical saturable absorber for ultrafast photonics operation and a stable all-optical pulse thresholder is demonstrated in Ref. [14]. Recent reports show that it can also be employed as an all-optical Kerr switcher and wavelength converter where modulated high-speed signals at a frequency up to 18 GHz are achieved [15], and it presents high stability under ambient conditions that can last for months [16]. New 2D material such as phosphorene is reported in the application of a robust delivery platform for cancer theranostics and development of reliable devices for optoelectronic applications [17,18]. There are also compounds with the form of MX_2, where M stands for the transition metal and X stands for the dichalcogenide element [19] and 2D layered metal dichalcogenide (LMD) such as

SnS_2 [20], MoS_2 [8], and WS_2 [19]. However up until now, there is no single material that is developed into the sole dominant material for the optoelectronic and photonic applications. This is due to the fact that various materials have different physical and chemical properties in terms of stability, electron mobility, on/off ratio, thickness-dependent bandgaps, etc.

Tin disulfide (SnS_2), which belongs to the extended families of LMD, has unique properties such as large surface areas, high on/off ratio, finite bandgap of ~2.35 eV, strong absorption property in the visible regime, high discharged capacity, and high carrier mobility, making it a suitable material for developing next-generation electronics or photonics devices [21,22]. It has been investigated as field effect transistors [23], photodetectors [20,24,25], photocatalysts [26,27], solar cells [28], etc. Particularly, the property of its strong absorption can be exploited as light–controlled–light all-optical devices.

In this paper, a light–controlled–light functionality by the structure of an MKR with SnS_2 is demonstrated where the transmitted signal power is controlled via the violet pump light power. The largest transmitted power variation rate ΔT versus violet light power is about 0.22 dB/mW, while the structure can run as fast as 3.2 ms. In addition, the light amplitude tuning experiment in the MKR with a SnS_2 structure enables a direct demonstration that resonances with a larger Q and a higher extinction ratio (ER) can yield a higher sensitivity. The paper is structured as follows: the structure fabrication of SnS_2-coated MKR is first elaborated, and then the experimental details, phenomenon, and discussion on the obtained results are presented. Simulations by the coupled mode theory are also carried out in order to uncover the physical mechanism of the observed phenomena. Afterwards, the response time of the device is measured. Lastly, the main results are compared with other types of structures, and some perspectives are provided.

2. DEVICE FABRICATION

In order to obtain the MKR with the SnS_2 structure, an MKR is first needed to be fabricated. The MF (which is utilized to form the MKR) fabrication starts with a standard SMF-28 (Corning) with a core diameter of 8 μm, and it is fabricated by the heat flame taper-drawing method [7]. Afterwards, the MF is assembled into an intertwisted MKR structure with the aid of translational stages and microscopes. The fabricated MKR is then packed onto a MgF_2 crystal substrate with a high degree of cleanliness.

Microscopic imaging and measurement of the optical transmission are performed for the MKR structure characterization. The microscopic image of the structure is shown in Fig. 1(a), which depicts the MKR structure with a diameter of $D \approx 480.6$ μm. The inset in Fig. 1(a) shows the waist region of the MF with a diameter of $d \approx 7.0$ μm. We can see from these images that the MF has a low surface roughness and the MKR is assembled with good quality. Transmission is measured by connecting a tunable laser source (TLS) to one end of the MKR, while the other end is connected to an optical spectrum analyzer (OSA). Figure 1(b) shows the measured transmission spectrum of the MKR from which we can deduce that the MKR has a free spectral range (FSR) of ~1.07,

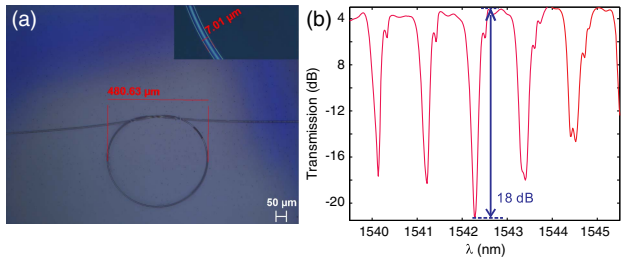

Fig. 1. (a) Microscopic images of the MKR with a loop diameter of $D \approx 480.6$ μm, and the inset shows the waist region of the MF with a diameter of $d \approx 7.0$ μm. (b) Transmission of the MKR structure where the largest obtained ER is ~18.0 dB at a resonance wavelength around 1542.3 nm.

a Q factor of ~40, 586, and an ER of ~18.0 dB at a resonance wavelength around 1542.3 nm.

The next step is to deposit the SnS_2 nanosheets onto the MKR, which has low-loss, high-Q-factor characteristics. The SnS_2 dispersions employed in our experiment are fabricated by the lithium ion intercalation exfoliation method with a concentration of 1 mg/mL. The SnS_2 nanosheets have finite lateral sizes of about 0.05–1 μm, while the thickness varies from 1 to 10 layers [29]. Raman and UV-Vis absorption spectra are performed for the characterization of SnS_2 nanosheets, and the results are shown in Fig. 2.

The Raman spectrum of SnS_2 shown in Fig. 2(a) depicts a peak around 313.8 cm^{-1}. It corresponds to the A_{1g} mode of the SnS_2, which is the signature of SnS_2 interlayer molecular oscillation [23]. Notice that the usual detected weak intralayer E_g mode in SnS_2 crystal Raman spectra is not found here in Fig. 2(a). It might be due to a too weak rejection of the Rayleigh-scattered radiation to be detected by the Raman sensor. The UV-Vis absorption spectrum is shown in Fig. 2(b), from which we can see that it has strong absorption at the wavelength ranging from 200 nm to 500 nm and a local peak around 250 nm. The absorption property is relatively strong at a wavelength of 405 nm, which corresponds to violet light [27].

After characterizing the SnS_2 dispersions, we then perform a ultrasonic treatment for ~30 min at a temperature of 25°C in order to obtain quasi-evenly distributed SnS_2 nanosheets. Immediately after the ultrasonic process is finished, a pipette is employed to transfer the dispersions to the arc areas of the MF away from the knot of the MKR. The reason for coating the SnS_2 away from the intertwisted knot is that the resonance condition might not be satisfied since too much of the

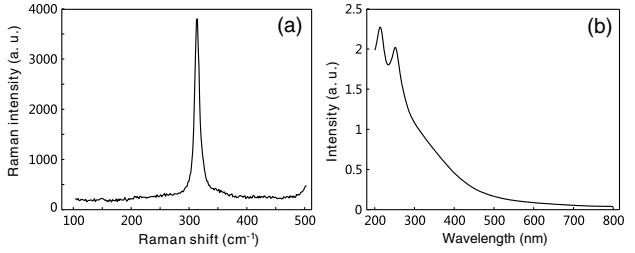

Fig. 2. (a) Raman spectrum of the SnS_2 nanosheets. (b) Absorption spectrum of the SnS_2 nanosheets.

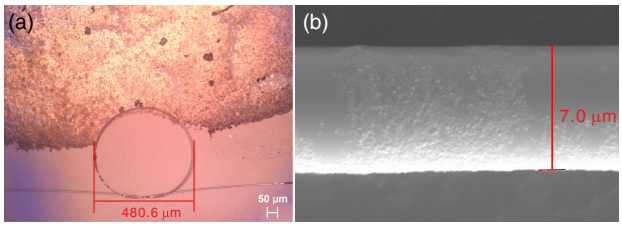

Fig. 3. (a) Microscopic image of the MKR coated with SnS_2 nanosheets. (b) SEM image of the MKR coated with SnS_2.

absorption will lead to a small fraction of the light being recirculated back to the loop. In addition, coating only the areas away from the knot, one makes sure that the deposition of the SnS_2 nanosheets will induce an increased loss factor to the resonator [30]. Consequently, it mainly affects the transmission amplitude of the resonance.

The MKR with the SnS_2 structure is built after the solvent is evaporated, and it reaches a stable state (usually it takes about several hours). A TLS and an OSA are employed for transmission measurement, which serves as a sign of whether the evaporation is finished or not since the output spectrum will have little variation when it is stable. Figure 3(a) shows a microscopic image of the final fabricated device where about one third of the area away from the knot is coated with SnS_2. Figure 3(b) shows an scanning electron microscope (SEM) image of a small part of the MKR circumference from which we can see that the SnS_2 nanosheets are successfully coated onto the MKR structure where the thickness varies from 100 nm to 300 nm. Optical characterization and external vertical violet pump light for MKR resonance amplitude tuning will be presented in the following section.

3. EXPERIMENTAL DETAILS, RESULTS, AND DISCUSSION

In this section, optical characterization of the MKR with and without SnS_2 will be presented. The experimental setup for the device characterization is shown in Fig. 4, where the sample is fixed at a basin made of UV adhesive. Light from TLS (ANDO-AQ4321D) is connected to one end of the MKR structure while the output is connected to an OSA (YOKOGAWA-AQ6317C). The 405 nm laser diode (LASEVER-LSR405NL) is placed vertically above the sample (either MKR with or without SnS_2) at a distance of ~10 cm, and it is focused by a cylindrical lens. The focused light then shines directly to the MKR areas centering in the arc area away from the knot.

Figure 5(a) shows the transmission spectrum of the MKR structure with and without SnS_2 at the off-state of the violet pump light. Qualitatively, there are several noticeable distinctions between the two curves. First, the overall transmission of the MKR with SnS_2 [green curve in Fig. 5(a)] is ~5.0 dB lower than that of the MKR without SnS_2 [red curve in Fig. 5(a)]. Second, the spectrum seems smoother in the case of the MKR with SnS_2 than in the case of MKR without SnS_2. Third, the resonance line shape is broadened in the case of the MKR with SnS_2 when compared with that in the case of MKR without SnS_2. As to the 5.0 dB in the transmission difference and the broadened resonance, these are mainly due to the increased loss factor brought by the deposition of SnS_2. In terms of the smoother curve, it indicates that there is only one dominant resonance condition satisfied in the MKR with SnS_2 structure while other possible resonances are suppressed due to the increased loss resulting from SnS_2. Similar phenomena of a smoother transmission curve after adding materials with absorption are also reported in Ref. [31]. In the case of the MKR without SnS_2, several resonances occurred. One dominant resonance, for which the mode-coupling efficiency is the highest among others, forms the comb-like shape of the resonance spectrum in the case of the MKR without SnS_2. Other minor resonances are shown as small dips in the spectrum as the one highlighted as the purple ellipse in Fig. 5(a). These are probably created by the slightly inhomogeneous properties of the MF with SnS_2 nanosheets. The inhomogeneous properties here refer to the quasi-periodically small diameter difference along the circumference of the MKR, which is caused by the manually pulling force pattern employed during the MF fabrication. Notice also that the λ_{res} position does not overlap between the two curves in Fig. 5(a). If one compares the λ_{res} corresponding to the maximum ER in the two cases, a red shift phenomenon in the MKR with SnS_2 will be observed. This indicates that the

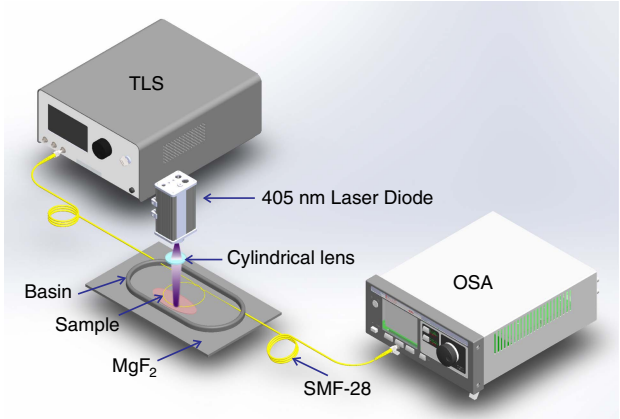

Fig. 4. Experimental setup for light amplitude tuning by violet pump light power.

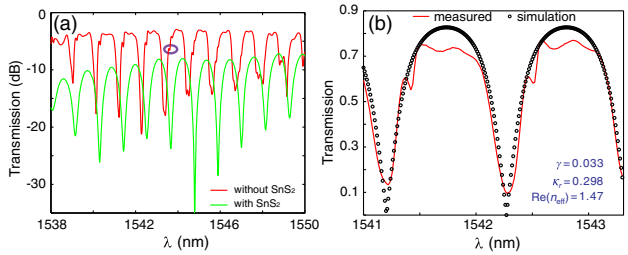

Fig. 5. (a) Transmission recorded from the MKR without SnS_2 (red curve) and the MKR with SnS_2 (green curve). The purple ellipse shows one minor resonance in the MKR without SnS_2. (b) Measured normalized transmission spectrum of the MKR without SnS_2 (red curve) and the corresponding fitted resonance curve (black circles). The fitted curve is obtained by setting $\gamma = 0.033$, $\kappa_r = 0.298$, and $\mathrm{Re}(n_{\mathrm{eff}}) = 1.47$.

resonance order and the mode effective index of the resonance in the two cases might not be the same.

Theoretically, there are ways of estimating the absorption induced by SnS_2, such as what is presented in Ref. [13], which is obtained via fitting the notch region of the spectrum. Simulations according to the coupled mode theory are performed to fit the experimental curves in Fig. 5(a). The comparison of the measured normalized transmission spectra with the fitted curves is shown in Figs. 5(b) and 6(a). The normalized experimental transmission spectra are normalized to the transmission obtained within the bare MF. The fitted curves are obtained according to the following equation based on the coupled mode theory [32,33]:

$$|T|^2 = (1-\gamma)\frac{2\kappa_r[1+\sin(\beta L)]}{1+\kappa_r^2+2\kappa_r\sin(\beta L)}, \quad (1)$$

where γ is the coupling loss due to the light scattering by the twisted knot and the attenuation brought by the MKR loop, and κ_r is the coupling coefficient that relates to the fractional coupling intensity at different ports of the MKR. The optimum value of the coupling depends mostly on the parameters of loss and the coupling coefficient. $\beta = (2\pi/\lambda)\mathrm{Re}(n_{\mathrm{eff}})$ is the propagation constant, λ is the resonance wavelength, and $\mathrm{Re}(n_{\mathrm{eff}})$ is the real part of the mode effective index. At the resonance, minima is achieved in Eq. (1). This condition and the experimentally measured FSR makes it possible to estimate the mode effective index $\mathrm{Re}(n_{\mathrm{eff}})$ and the corresponding resonance order. The fitted curve results are shown as black circles in Figs. 5(b) and 6(a), from which we can see that there is good agreement between the simulation and experiment results. For the fitted transmission of the MKR [black circles in Fig. 5(b)], the estimated $\mathrm{Re}(n_{\mathrm{eff}}) = 1.47$, $\gamma = 0.03$, and $\kappa_r = 0.29$, and its corresponding resonance order is 1445. For the fitted transmission of the MKR with SnS_2 [black circles in Fig. 6(a)], the estimated $\mathrm{Re}(n_{\mathrm{eff}}) = 1.42$, $\gamma = 0.67$, and $\kappa_r = 0.21$, and its corresponding resonance order is 1393. The difference in the resonance order and mode effective index contributes to the resonance wavelength difference in the structure of the MKR with and without SnS_2. These simulated results indicate that absorption increases after the deposition of the SnS_2 nanosheet since the coupling loss changes from $\gamma = 0.03$ (MKR without SnS_2) up to $\gamma = 0.67$ (MKR with SnS_2). The simulated results also indicate that the absorption is increased after the deposition of SnS_2 since the coupling loss increases from $\gamma = 0.03$ (MKR without SnS_2) up to $\gamma = 0.67$ (MKR with SnS_2).

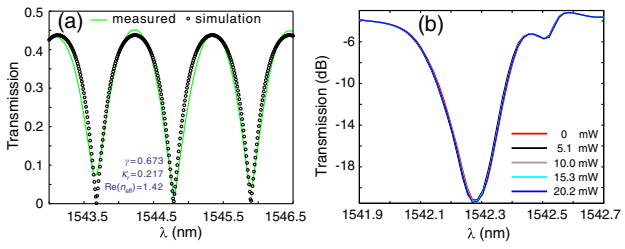

Fig. 6. (a) Measured normalized transmission spectra of the MKR with SnS_2 (green curve) and the corresponding fitted resonance curve (black circles). The fitted curve is obtained by setting $\gamma = 0.673$, $\kappa_r = 0.217$, and $\mathrm{Re}(n_{\mathrm{eff}}) = 1.42$. (b) Transmission of the MKR structure at different external violet pump light powers. The red, black, brown, cyan, and blue curves correspond to the transmission with external violet pump power of 0, 5.1, 10, 15.3, and 20.2 mW, respectively.

Table 1. Resonance Properties of Structures in the MKR with and without SnS_2

Structure	λ_{res} (nm)	$\mathrm{ER}_{\mathrm{max}}$ (dB)	Q	FSR (nm)
MKR without SnS_2	1542.3	18.0	40586	1.07
MKR with SnS_2	1544.7	26.6	59415	1.11

Quantitatively, the diameters of the MF and the MKR have hardly changed after coating with SnS_2, which shows the stability of the device [in Figs. 1(a) and 3]. Other resonance properties of the MKR with and without SnS_2 are summarized in Table 1. The resonance wavelength λ_{res} of the maximum ER (18.0 dB) takes place at 1542.3 nm in the MKR without SnS_2. However, in the case of the MKR with SnS_2, the λ_{res} of the maximum ER (26.6 dB) takes place at 1544.7 nm. The λ_{res} of the maximum ER takes place at a larger wavelength, which might be due to the difference in the resonance order and its mode effective index, which is suggested by the fitted parameters of the resonance notch in Figs. 5(b) and 6(a) [6,34]. The resonance ER is higher in the MKR with SnS_2 than in the case of the MKR without SnS_2. This indicates that in the case of no SnS_2, the resonator might be at a state of undercoupling. However, in the case of the MKR with SnS_2, the resonator might be at a state of critical coupling, which will be further verified by the decreased ER phenomenon induced via the violet pump light demonstrated in the following. The change of the resonance condition in the MKR with SnS_2 might be due to the increased loss factor (estimated $\gamma = 0.67$ by coupled mode theory) brought by the SnS_2 nanosheets via light scattering and the absorption effect [34]. Thanks to the increase of ER, the MKR with the SnS_2 structure yields a larger resonance Q ($\sim 59,415$) than that of the MKR without SnS_2 ($Q \sim 40,586$). In terms of the resonance FSR, it is 1.07 for the MKR without SnS_2, while for the MKR with SnS_2 it is 1.11. The small variation in FSR might be due to the small changes in the resonance conditions, such as coupling loss and coupling coefficients after coating with SnS_2 [6].

The violet pump light for the resonance amplitude tuning experiment is first performed on the MKR without the SnS_2 structure with the violet pump power varying at 0, 5.1, 10, 15.3, and 20.2 mW. The output transmission spectra are recorded, and the result at around 1542.3 nm is shown in Fig. 6(b). From Fig. 6(b), we can see that the transmitted light amplitude variation ΔT at the resonance dip wavelength λ_{res} is smaller than 0.1 dB, and hardly no shift can be found in the λ_{res}. These results indicate that an MKR made of only silica-based MF cannot enable light amplitude tuning of the MKR resonance.

By employing the same experimental setup (Fig. 4) and the same violet light power variation, the violet pump light for resonance light amplitude tuning is then performed on the MKR with the SnS_2 structure. The measured output spectra around the wavelengths of 1544.7 nm and 1569.6 nm are shown in Figs. 7(a) and 7(b), respectively. With the increase of violet light power, the transmitted optical power increases

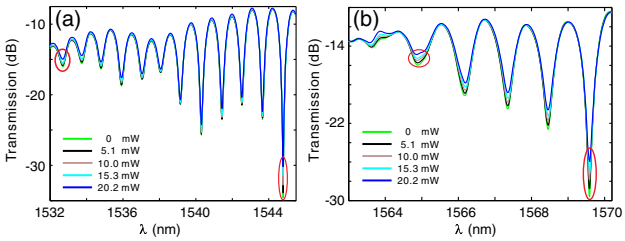

Fig. 7. Transmission spectrum of the MKR with SnS_2 under different violet pump power excitation within a wavelength range of (a) 1532 nm to 1545 nm, while the two modes highlighted with red ellipses are around 1533 nm and 1544.7 nm, and (b) 1563 nm to 1570 nm, while the two modes highlighted with red ellipses are around 1564 nm and 1569.6 nm.

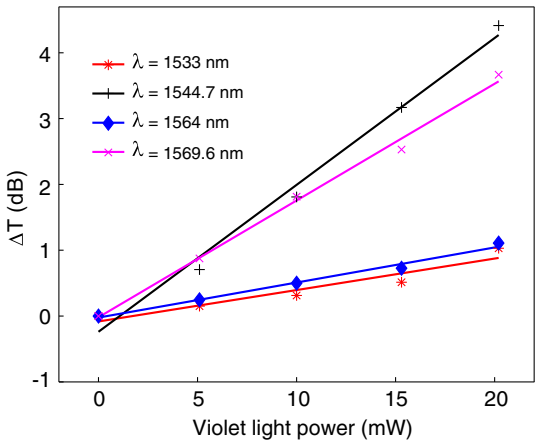

Fig. 8. Linear fit of ΔT versus violet light power for four different resonances at $\lambda_{res} = 1533$ nm (red curve with a correlation coefficient of 93.8%), $\lambda_{res} = 1544.7$ nm (black curve with a correlation coefficient of 98.4%), $\lambda_{res} = 1564$ nm (blue curve with a correlation coefficient of 98.4%), and $\lambda_{res} = 1569.6$ nm (pink curve with a correlation coefficient of 99.5%).

corresponding to a decrease in the resonance ER. The largest ΔT of ~4.5 dB is obtained at a wavelength of 1544.7 nm, shown as the red ellipse in Fig. 7(a). The decreasing ER might indicate that the resonance condition changes from critical coupling to the undercoupling state under violet light excitation. The physical mechanism favoring this change of the resonance condition might probably be explained as follows: the strong absorption property of SnS_2 at 405 nm violet light will lead to the excitation of electron–hole pairs in SnS_2 nanosheets. These photon-generated carriers will then lead to both the real and imaginary parts of the index variation in SnS_2 nanosheets. As to the real part of the index variation in SnS_2 nanosheets, it relates and manifests as a wavelength shift in the resonance wavelength. However, no significant resonance wavelength shift can be found in Fig. 7. This might be due to the fact that the real part of the index variation is not big enough to induce a detectable mode effective index variation of the resonance. The detection of the resonance wavelength shift depends not only on the surrounded material index variations, but it also greatly relates to how sensitive the mode effective index is. On the other hand, the changes of the imaginary part of the SnS_2 nanosheet index might lead to variations in resonance conditions. Consequently, the transmitted power is varied accordingly. With the increase of the pump light power excitation, the concentration of the photon-excited carriers increases. This will then lead to an increase in the coupling loss factor for the MKR. For the resonance modes that are at the critical coupling state under no pump light excitation, an increase of the coupling loss factor will deviate the resonance state out of critical coupling [34]. Consequently, a decrease of the resonance ER or an increase of the transmitted power can be found at the vicinity of the resonance wavelength.

Within a signal light wavelength ranging from 1520 nm to 1620 nm, multiple resonances can be exploited for the amplitude tuning through the violet light absorption property by SnS_2 nanosheets. In order to investigate how the ΔT changes with respect to different resonance properties, we outline four different resonances (highlighted with red ellipses in Fig. 7) for detailed analysis. Correspondingly, the linear fit of ΔT versus violet light power for these resonances is shown in Fig. 8. Table 2 summarizes the resonance properties and the obtained ΔT variation rate associated with these resonances.

Table 2. Properties and the Obtained ΔT Variation Rate Associated with the Four Highlighted Resonances in Fig. 7

λ_{res} (nm)	Q	ER	ΔT at 20.2 mW (dB)	$\frac{\Delta T}{\text{Violet Power}}$ (dB/mW)
1533	1915	3.7	1.0	0.053
1544.7	**59415**	**26.6**	**4.5**	**0.22**
1564	2016	4.2	1.1	0.053
1569.6	*20652*	*19.2*	*3.7*	*0.177*

The largest ΔT variation rate with respect to violet light power is 0.22 dB/mW with a correlation coefficient of 98.4%, which corresponds to the black curve that has the steepest slope in Fig. 8. It is obtained at ~1544.7 nm, which corresponds to a resonance with the highest Q (59,415) and the largest ER (26.6 dB), as is shown in bold font in Table 2. The second largest ΔT variation rate with respect to violet light power is 0.177 dB/mW with a correlation coefficient of 99.5% (pink curve in Fig. 8), which corresponds to a resonance with a lower Q (20,652) and a smaller ER (19.2 dB) at λ_{res} of 1569.6 nm, as is shown in italic font in Table 2. The other ΔT variation rates with respect to violet light power corresponding to resonances that have a poor Q and a smaller resonance ER at 1533 nm with a correlation coefficient of 93.8% and at 1564 nm with a correlation coefficient of 98.4% are both 0.053 dB/mW. The above analysis for the four different highlighted resonance properties' variation (in Figs. 7 and 8) under the same external violet light excitation shows a clear fact that resonances with higher Q and larger ER can lead to higher sensitivities for the resonance properties' variation rate. This can be understood by the fact that a resonance with a high Q and ER will have a large amount of light energy stored inside the structure, which will then enhance the light–matter interaction. The enhanced light–matter interaction will then lead to a

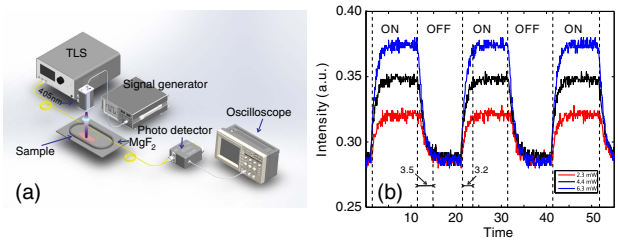

Fig. 9. (a) Experimental setup for device response time measurement. (b) Response time of the device at a probe wavelength of 1548 nm with a violet light power of 2.3, 4.4, and 6.3 mW.

higher sensitivity of the resonance property variation rate with respect to the external stimuli.

In order to further characterize the device of the MKR with SnS_2, an experiment aiming at measuring its response time is performed, where the experimental setup is shown in Fig. 9(a). A signal generator is employed for the on and off state control of the violet pump light signal. A TLS is connected to the input facet of the sample. The transmitted light from the sample then passes through a photodetector, and finally it is collected by an oscilloscope.

In order to investigate whether the device response time relates to the violet pump light power, experiments of varying the violet light power at 2.3 mW, 4.4 mW, and 6.3 mW at a signal wavelength of 1521 nm are carried out. The output of the signal generator is chosen as a 20 ms periodic square wave. The response obtained from the oscilloscope is shown in Fig. 9(b). It shows a rise time t_r of ~3.2 ms and a fall time t_f of ~3.5 ms. The response time measurement processes are repeated for several tens of periods for different violet light powers. They all show good repeatability. The averaged rise time of the sample is ~3.5 ms, and the averaged fall time is ~3.7 ms among different measurements. The response time of the above measurements has already taken into account the response time of the system including the photodetector and the oscilloscope. Therefore, this response time is a lower limit of the MKR with the SnS_2 structure. Further improvement such as developing a more homogeneous material deposition and better control over the deposition thickness might lead to a decrease of the response time.

Regarding sensitivity enhancement of the ΔT variation with respect to violet pump light excitation in the MKR coated with SnS_2, the MKR without SnS_2 has a ΔT of less than 0.1 dB under 20.2 mW violet pump light excitation, whereas the MKR with SnS_2 yields a ΔT of 4.5 dB. As a consequence, the MKR with SnS_2 has over a 45-fold enhancement in the ΔT variation under violet pump light excitation. Table 3 shows the performances of different types of light–control–light structures. In terms of sensitivity, the MKR with SnS_2 demonstrated in this paper (bold font in Table 3) outperforms other configurations. The response time of the MKR with SnS_2 yields a better result than those structures such as liquid crystals [35] and $MoSe_2$ [36]. Consequently, the SnS_2-coated MKRs demonstrated here, if they are further improved by optimized design for higher sensitivity and smaller response time, might be used as optical switches, multichannel amplitude modulators, and handheld fiber sensors. As an optical switch, the structure might need to be further optimized for internally pump light excitation in order to facilitate the control of switching on and off the resonance, and the response time should be reduced by improving the thickness homogeneity and the quality of SnS_2 deposition. As multichannel amplitude modulators, an alternative geometry for adding the probe lights such as multiple monochromatic continuous waves at the corresponding MKR resonance wavelength might be a good choice. For the handheld fiber sensors, a more rigid assembling of the structure into a device should be developed.

Table 3. Performances Comparison of Different Light–Control–Light Structures

Type of Structure	Sensitivity (dB/mW)	Response Time
MKR with liquid crystals [35]	0.15 at 25°C	5 s
MKR with graphene [3]	0.02	—
MF with $MoSe_2$ [36]	0.165	0.6 s
MF with graphene [37]	0.2	—
MF with bilayer graphene [38]	0.007	1×10^{-6} s
SnS_2 + MKR (this paper)	**0.22**	**3.2×10^{-3} s**

4. CONCLUSION

In conclusion, we have demonstrated that by coating an MKR with 2D material SnS_2 nanosheets, light–control–light functionality can be realized. Thanks to the multiresonance nature of the MKR, the sensitivity variations of resonances with different properties under the same external stimuli are demonstrated. It shows that a resonance of a higher Q and larger ER can lead to a higher sensitivity. The highest ΔT variation rate with respect to violet pump light power obtained in the MKR with the SnS_2 structure is 0.22 dB/mW, corresponding to an MKR with a loop diameter of 480.6 μm that is made of a 7.0 μm diameter MF. It is obtained at λ_{res} around 1544.7 nm with a Q of 59,415 and an ER of 25.6 dB. In terms of response time, the structure can run as fast as ~3.2 ms. The demonstrated light–control–light all-optical structure has the advantages of short response time, low cost, easy fabrication, and compatibility with fiber optics. Therefore, it might be a good candidate for developing fiber-compatible devices with other functionalities.

Funding. National Natural Science Foundation of China (NSFC) (61475066, 61505069, 61675092, 61705087, 61705089, 61775084); Guangdong Special Support Program (2016TQ03X962); Natural Science Foundation of Guangdong Province (2015A030306046, 2016A030310098, 2016A030311019); Science and Technology Project of Guangzhou (201605030002, 201607010134, 201704030105); Science and Technology Projects of Guangdong Province (2014B090905001); Rail Transit Healthy Operation Cooperative Innovation Center of Zhuhai (55560307).

†These authors contributed equally to this work.

REFERENCES

1. B. Behroozpour, P. A. M. Sandborn, N. Quack, T. J. Seok, Y. Matsui, M. C. Wu, and B. E. Boser, "Electronic-photonic integrated circuit for 3D microimaging," IEEE J. Solid-State Circuits **52**, 161–172 (2017).
2. K. A. Williams, "Prospects for electronic photonic integration," in *Integrated Photonics Research (IPR)* (Optical Society of America, 2017), paper IW3A.1.
3. Y. Meng, L. Deng, Z. Liu, H. Xiao, X. Guo, M. Liao, A. Guo, T. Ying, and Y. Tian, "All-optical tunable microfiber knot resonator with graphene-assisted sandwich structure," Opt. Express **25**, 18451–18461 (2017).
4. X. Jiang, Q. Yang, G. Vienne, Y. Li, L. Tong, J. Zhang, and L. Hu, "Demonstration of microfiber knot laser," Appl. Phys. Lett. **89**, 143513 (2006).
5. X. Jiang, Y. Chen, G. Vienne, and L. Tong, "All-fiber add–drop filters based on microfiber knot resonators," Opt. Lett. **32**, 1710–1712 (2007).
6. X. Jiang, L. Tong, G. Vienne, X. Guo, A. Tsao, Q. Yang, and D. Yang, "Demonstration of optical microfiber knot resonators," Appl. Phys. Lett. **88**, 223501 (2006).
7. L. Tong, F. Zi, X. Guo, and J. Lou, "Optical microfibers and nanofibers: a tutorial," Opt. Commun. **285**, 4641–4647 (2012).
8. H. Zhang, S. B. Lu, J. Zheng, J. Du, S. C. Wen, D. Y. Tang, and K. P. Loh, "Molybdenum disulfide (MoS_2) as a broadband saturable absorber for ultra-fast photonics," Opt. Express **22**, 7249–7260 (2014).
9. M. Liu, X. Zheng, Y. Qi, H. Liu, A. Luo, Z. Luo, W. Xu, C.-J. Zhao, and H. Zhang, "Microfiber-based few-layer MoS_2 saturable absorber for 2.5 GHz passively harmonic mode-locked fiber laser," Opt. Express **22**, 22841–22846 (2014).
10. A. Luo, M. Liu, X. Wang, Q. Ning, W. Xu, and Z. Luo, "Few-layer MoS_2-deposited microfiber as highly nonlinear photonic device for pulse shaping in a fiber laser [Invited]," Photon. Res. **3**, A69–A78 (2015).
11. L. Gai, J. Li, and Y. Zhao, "Preparation and application of microfiber resonant ring sensors: a review," Opt. Laser Technol. **89**, 126–136 (2017).
12. K. S. Novoselov, A. K. Geim, S. V. Morozov, D. Jiang, Y. Zhang, S. V. Dubonos, I. V. Grigorieva, and A. A. Firsov, "Electric field effect in atomically thin carbon films," Science **306**, 666–669 (2004).
13. C. Qiu, Y. Yang, C. Li, Y. Wang, K. Wu, and J. Chen, "All-optical control of light on a graphene-on-silicon nitride chip using thermo-optic effect," Sci. Rep. **7**, 17046 (2017).
14. Y. Song, Z. Liang, X. Jiang, Y. Chen, Z. Li, L. Lu, Y. Ge, K. Wang, J. Zheng, S. Lu, J. Ji, and H. Zhang, "Few-layer antimonene decorated microfiber: ultra-short pulse generation and all-optical thresholding with enhanced long term stability," 2D Mater. **4**, 045010 (2017).
15. Y. Song, Y. Chen, X. Jiang, W. Liang, K. Wang, Z. Liang, Y. Ge, F. Zhang, L. Wu, J. Zheng, J. Ji, and H. Zhang, "Nonlinear few-layer antimonene-based all-optical signal processing: ultrafast optical switching and high-speed wavelength conversion," Adv. Opt. Mater. **6**, 1701287 (2018).
16. L. Lu, X. Tang, R. Cao, L. Wu, Z. Li, G. Jing, B. Dong, S. Lu, Y. Li, Y. Xiang, J. Li, D. Fan, and H. Zhang, "Broadband nonlinear optical response in few-layer antimonene and antimonene quantum dots: a promising optical Kerr media with enhanced stability," Adv. Opt. Mater. **5**, 1700301 (2017).
17. W. Tao, X. Zhu, X. Yu, X. Zeng, Q. Xiao, X. Zhang, X. Ji, X. Wang, J. Shi, H. Zhang, and L. Mei, "Black phosphorus nanosheets as a robust delivery platform for cancer theranostics," Adv. Mater. **29**, 1603276 (2017).
18. S. C. Dhanabalan, J. S. Ponraj, Z. Guo, S. Li, Q. Bao, and H. Zhang, "Emerging trends in phosphorene fabrication towards next generation devices," Adv. Sci. **4**, 1600305 (2017).
19. B. Peng, H. Zhang, H. Shao, Y. Xu, X. Zhang, and H. Zhu, "Thermal conductivity of monolayer MoS_2, $MoSe_2$, and WS_2: interplay of mass effect, interatomic bonding and anharmonicity," RSC Adv. **6**, 5767–5773 (2016).
20. J. Xia, D. Zhu, L. Wang, B. Huang, X. Huang, and X. Meng, "Large-scale growth of two-dimensional SnS_2 crystals driven by screw dislocations and application to photodetectors," Adv. Funct. Mater. **25**, 4255–4261 (2015).
21. J. Fang, M. Chen, and Z. Fang, "Thickness-dependent photoelectrochemical property of tin disulphide nanosheets," Micro Nano Lett. **12**, 344–346 (2017).
22. Y. Huang, E. Sutter, J. T. Sadowski, M. Cotlet, O. L. A. Monti, D. A. Racke, M. R. Neupane, D. Wickramaratne, R. K. Lake, B. A. Parkinson, and P. Sutter, "Tin disulfide—an emerging layered metal dichalcogenide semiconductor: materials properties and device characteristics," ACS Nano **8**, 10743–10755 (2014).
23. H. S. Song, S. L. Li, L. Gao, Y. Xu, K. Ueno, J. Tang, Y. B. Cheng, and K. Tsukagoshi, "High-performance top-gated monolayer SnS_2 field-effect transistors and their integrated logic circuits," Nanoscale **5**, 9666–9670 (2013).
24. G. Su, V. G. Hadjiev, P. E. Loya, J. Zhang, S. Lei, S. Maharjan, P. Dong, P. M. Ajayan, J. Lou, and H. Peng, "Chemical vapor deposition of thin crystals of layered semiconductor SnS_2 for fast photodetection application," Nano Lett. **15**, 506–513 (2015).
25. Y. Tao, X. Wu, W. Wang, and J. Wang, "Flexible photodetector from ultraviolet to near infrared based on a SnS_2 nanosheet microsphere film," J. Mater. Chem. C **3**, 1347–1353 (2015).
26. L. A. Burton, T. J. Whittles, D. Hesp, W. M. Linhart, J. M. Skelton, B. Hou, R. F. Webster, G. O'Dowd, C. Reece, D. Cherns, D. J. Fermin, T. D. Veal, V. R. Dhanak, and A. Walsh, "Electronic and optical properties of single crystal SnS_2: an earth-abundant disulfide photocatalyst," J. Mater. Chem. A **4**, 1312–1318 (2016).
27. W. Du, D. Deng, Z. Han, W. Xiao, C. Bian, and X. Qian, "Hexagonal tin disulfide nanoplatelets: a new photocatalyst driven by solar light," CrystEngComm **13**, 2071–2076 (2011).
28. J. Ahn, M. Lee, H. Heo, J. Ho Sung, K. Kim, H. Hwang, and M. Jo, "Deterministic two-dimensional polymorphism growth of hexagonal n-type SnS_2 and orthorhombic p-type SnS crystals," Nano Lett. **15**, 3703–3708 (2015).
29. www.mukenano.com.
30. K. S. Lim, A. A. Jasim, S. S. A. Damanhuri, S. W. Harun, B. M. Azizur Rahman, and H. Ahmad, "Resonance condition of a microfiber knot resonator immersed in liquids," Appl. Opt. **50**, 5912–5916 (2011).
31. Y. Chen, Q. Han, T. Liu, X. Lan, and H. Xiao, "Optical fiber magnetic field sensor based on single-mode–multimode–single-mode structure and magnetic fluid," Opt. Lett. **38**, 3999–4001 (2013).
32. Y. Wang, X. Gan, C. Zhao, L. Fang, D. Mao, Y. Xu, F. Zhang, T. Xi, L. Ren, and J. Zhao, "All-optical control of microfiber resonator by graphene's photothermal effect," Appl. Phys. Lett. **108**, 171905 (2016).
33. L. F. Stokes, M. Chodorow, and H. J. Shaw, "All-single-mode fiber resonator," Opt. Lett. **7**, 288–290 (1982).
34. M. O. Stetsenko, A. A. Voznyi, V. V. Kosyak, S. P. Rudenko, L. S. Maksimenko, B. K. Serdega, and A. S. Opanasuk, "Plasmonic effects in tin disulfide nanostructured thin films obtained by the close-spaced vacuum sublimation," Plasmonics **12**, 1213–1220 (2017).
35. V. K. S. Hsiao, Z. Li, Z. Chen, P. Peng, and J. Tang, "Optically controllable side-polished fiber attenuator with photoresponsive liquid crystal overlay," Opt. Express **17**, 19988–19995 (2009).
36. D. Zhang, H. Guan, W. Zhu, J. Yu, H. Lu, W. Qiu, J. Dong, J. Zhang, Y. Luo, and Z. Chen, "All light-control-light properties of molybdenum diselenide ($MoSe_2$)-coated-microfiber," Opt. Express **25**, 28536–28546 (2017).
37. J. Chen, B. Zheng, G. Shao, S. Ge, F. Xu, and Y. Lu, "An all-optical modulator based on a stereo graphene–microfiber structure," Light Sci. Appl. **4**, e360 (2015).
38. Z. Liu, M. Feng, W. Jiang, W. Xin, P. Wang, Q. Sheng, Y. Liu, D. Wang, W. Zhou, and J. Tian, "Broadband all-optical modulation using a graphene-covered-microfiber," Laser Phys. Lett. **10**, 065901 (2013).